AGU ADVANCING EARTH AND SPACE SCIENCE

JGR Atmospheres

RESEARCH ARTICLE
10.1029/2022JD037114

Key Points:

- Diurnal clockwise rotation in the low-level winds is found to be linked to an around-noon rainfall peak on southern Hainan Island (HNI) in June
- Downwind advection of the upstream boundary layer inertial oscillations is responsible for the around-noon rainfall peak over HNI
- A gap across Annamite Range of Indochina Peninsula amplifies and transports boundary layer inertial oscillation signals downstream

Correspondence to:
M. Xue,
mxue@ou.edu

Citation:
Wang, X., Xue, M., Zhu, K., Zhang, Y., & Fan, Z. (2022). Diurnal variation of summer monsoon season precipitation over southern Hainan Island, China: The role of boundary layer inertial oscillations over Indochina Peninsula. *Journal of Geophysical Research: Atmospheres*, *127*, e2022JD037114. https://doi.org/10.1029/2022JD037114

Received 14 MAY 2022
Accepted 10 NOV 2022

Author Contributions:
Conceptualization: Xiucheng Wang, Ming Xue
Formal analysis: Xiucheng Wang
Investigation: Xiucheng Wang
Methodology: Xiucheng Wang, Ming Xue
Resources: Kefeng Zhu
Software: Xiucheng Wang, Yuehan Zhang, Ziqi Fan
Supervision: Ming Xue
Validation: Xiucheng Wang
Writing – original draft: Xiucheng Wang
Writing – review & editing: Ming Xue

Diurnal Variation of Summer Monsoon Season Precipitation Over Southern Hainan Island, China: The Role of Boundary Layer Inertial Oscillations Over Indochina Peninsula

Xiucheng Wang[1,2], Ming Xue[1,3], Kefeng Zhu[4], Yuehan Zhang[1], and Ziqi Fan[1]

[1]Key Laboratory of Mesoscale Severe Weather, Ministry of Education and School of Atmospheric Sciences, Nanjing University, Nanjing, China, [2]Meteorological Center, Northwest Air Traffic Management Bureau, Civil Aviation Administration of China, Xi'an, China, [3]Center for Analysis and Prediction of Storms and School of Meteorology, University of Oklahoma, Norman, OK, USA, [4]Key Laboratory of Transportation Meteorology of China Meteorological Administration, Nanjing Joint Institute for Atmospheric Sciences, Nanjing, China

Abstract In June after the onset of the East Asian summer monsoon season, rainfall on the south side of Hainan Island (HNI) of China exhibits a trimodal pattern with an unusual peak near noon. A typical case of 20 June 2017 is chosen to analyze the mechanisms through a convection-permitting simulation together with rainfall observations. Clockwise rotation in low-level winds is found at and off the coast of south HNI, leading to maximum onshore southwesterly winds in the late morning that is closely linked to the diurnal variation of rainfall. The offshore diurnal variations of low-level winds are tracked upstream and attributed to boundary layer inertial oscillations over the inland plain of Indochina Peninsula. In addition, a short wide gap comprised mostly of hills lower than 700 m is located across the higher Annamite Range along the east coast of the Peninsula, right upstream of HNI. Nocturnal boundary layer low-level jet (LLJ) forming over the plain passes through the gap with significant acceleration due to gap channeling and downslope flow effects, reaching peak intensity off the Peninsula coast at around 09 local standard time (LST). The enhanced LLJ propagates downstream towards HNI and impinges on the mountains at around 12 LST when rainfall reaches peak there. As the inertial-oscillation-indued perturbation winds approaching the Island weaken and eventually reverse direction, lifting weakens and low-level stability increases as descending motion develops offshore. Rainfall on the southern Island therefore dissipates in late afternoon.

Plain Language Summary In June after the onset of East Asian summer monsoon, rainfall on southern Hainan Island (HNI) of China has an unusual peak near noon. A representative case is numerically simulated at 2 km horizontal grid spacing and analyzed. It is found that the diurnal variation of rainfall is closely linked to diurnal variation of low-level onshore winds which reach peak intensity around noon, and the source of such variations can be tracked upstream to the inland plain of Indochina Peninsula (ICP). Over the plain, afternoon boundary layer mixing causes low-level wind speed minimum while boundary layer low-level jet reaches peak speed in early morning due to inertial oscillation after the boundary layer flow becomes freed of the surface friction when mixing is shut off. The peak perturbation wind is advected toward HNI, and reaches the Island around noon. The lifting by mountains on southern HNI of the intensified low-level winds causes peak rainfall there around noon. In the afternoon, the perturbation winds weaken and eventually reverse direction, causing dissipation of rainfall. In addition, the low-level flow is accelerated when it passes through a gap in the coastal Annamite Range of ICP, amplifying the effect of inertial oscillations.

1. Introduction

East Asian summer monsoon (EASM) is one of the most significant large-scale weather processes during warm season in East Asia. EASM usually commences abruptly over Indochina Peninsula (ICP hereafter) and South China Sea (SCS) around mid-May (Ding & Chan, 2005). After its onset, EASM advances northeastward intermittently and affects local weather as an important contributor of momentum, moisture, and heat. Fueled by strong low-level southwesterlies and ample moisture and heat originally from EASM, notable monsoonal rain belts such as Meiyu can evolve through interactions among the EASM, the western Pacific subtropical high, and midlatitude disturbances.

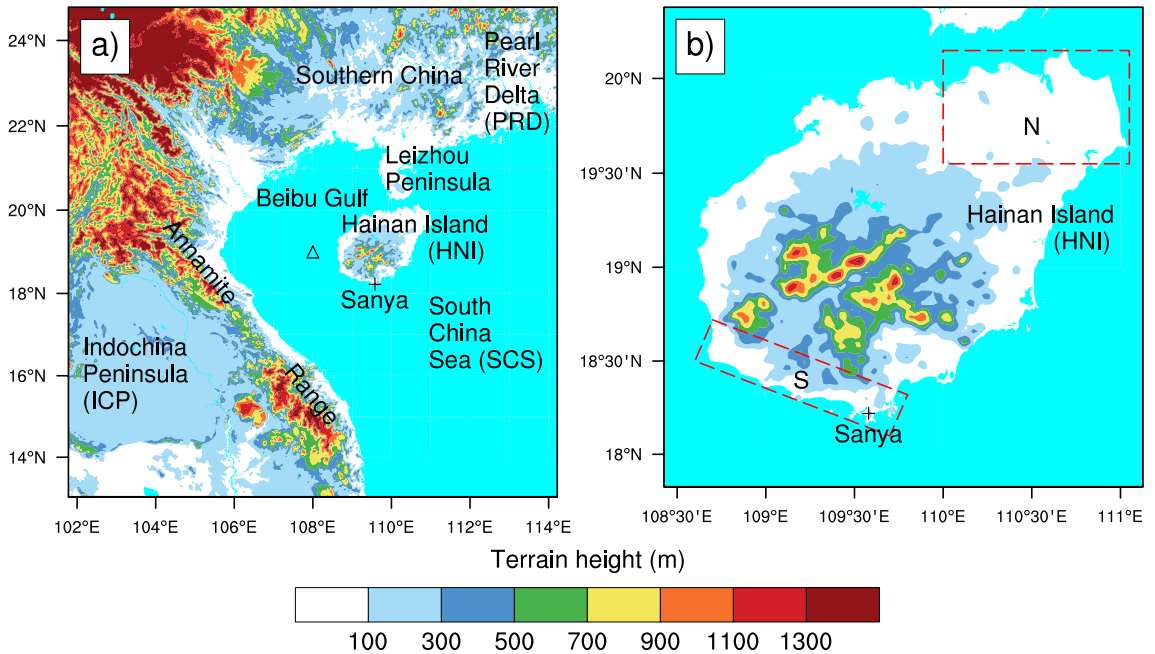

Figure 1. (a) Simulation model domain and terrain height (shaded). Locations of Hainan Island (HNI), Leizhou Peninsula, Pearl River Delta (PRD), Beibu Gulf, southern China, South China Sea (SCS), Indochina Peninsula (ICP), and Annamite Range are also labeled in the figure. The plus marker represents Sanya station. The unfilled triangle denotes the center of the model domain. (b) Terrain height of HNI (shaded) with Sanya station marked with a "+." The dashed red boxes labeled S and N are the regions selected to calculate the diurnal cycles of rainfall in Figure 2.

Under the influence of the prevailing low-level southwesterly winds associated with EASM, pronounced diurnal cycles of rainfall have been observed in southern China and the northern SCS (Chen et al., 2018; Wang et al., 2021; Yin et al., 2009; Yu et al., 2007). Four distinct diurnal cycle patterns of rainfall have been identified. The first pattern with a single afternoon peak is the most common in southern China, and has been observed in southern inland China (Yu et al., 2007), northern Hainan Island (Zhu et al., 2017) (HNI hereafter) and Leizhou Peninsula (Li et al., 2019). The second pattern with a primary afternoon peak and a secondary early-morning or late-night peak is also widespread, mostly in the coast-inland transition region and on windward mountains (Chen et al., 2018), such as the inland Pearl River Delta region near south China coast (Chen et al., 2014). The third pattern with a single early-morning peak mostly occurs offshore of southern China, while the fourth pattern with a primary early-morning peak and a secondary afternoon peak frequently appears along the coastline (Chen et al., 2018; Li et al., 2019).

The HNI (see Figure 1), a mesoscale tropical island located in the northern part of the SCS facing Leizhou Peninsula to the north, has a near-oval shape with a major axis of about 240 km in length extending southwest-northeastwards, and a minor axis of around 210 km in width. Its topographic feature consists of mountains with peaks of more than 1,800 m in the south and low plains in the north. Beibu Gulf and the neighboring sea separate the Island from the mainland of China with a narrow strait of about 30 km wide between the Island and Leizhou Peninsula. On the west side between the Island and the ICP is a broad strait of about 240 km wide. During EASM season, low-level prevailing winds over HNI are mostly southwesterly except for days affected by tropical cyclones from the east and by midlatitude disturbances (e.g., strong cold front) from the north.

Patterns of diurnal cycle of rainfall differ sharply between the northern and southern HNI during EASM season. Based on 10-year climatology, in June northern HNI is characterized by a clear single afternoon peak whereas the southern HNI coastal region exhibits a triple-peak pattern with a primary early-morning peak at 04 local standard time (LST) and a secondary peak near noon and a weakest peak at 17 LST (Figure 2). The single afternoon peak in northern HNI has been suggested to be caused by strong convergence between sea breeze fronts from the east and west coasts (Liang & Wang, 2017; Zhu et al.,2017, 2020). The triple-peak pattern in southern HNI is unique among the patterns found in southern China, especially the peak around noon. The early morning peak is also found in other coastal regions of south China during EASM season, and has been suggested to be

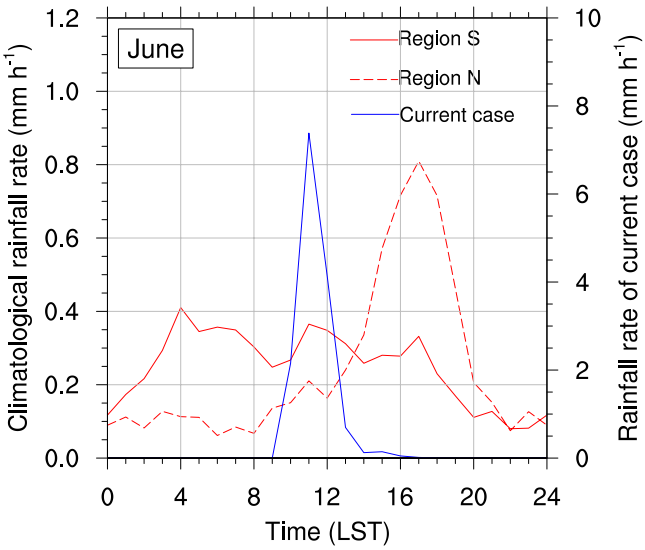

Figure 2. 10-year (2009–2018) mean diurnal cycles of rainfall in June in regions *S* and *N* as labeled in Figure 1b of Hainan Island. The observed rainfall of the current case from 00 LST 20 June to 00 LST 21 June in region *S* is overlaid in blue.

due to the convergence between nocturnal offshore land breeze and onshore southwesterly winds (Chen et al.,2014, 2016; Li et al., 2019). Prior studies on HNI rainfall (Liang & Wang, 2017; Zhang et al., 2014) suggest that a similar mechanism is at work in southern HNI, which is further enhanced by the mountains near the island south coast. The cause of the peak near noon has not been investigated in previous studies, however, the underlying mechanism is unclear.

Aside from land and sea breezes, marine boundary layer jet and the associated convergence lifting by differential friction at the coast and lifting by coastal barrier have been suggested to be an important contributor to rainfall near south China coast (Chen et al., 2015; Du & Chen, 2019; Du et al., 2020; Li et al., 2019). With this mechanism, peak rainfall should occur when the boundary layer jet is strongest. Du et al. (2020) proposed that boundary layer inertial oscillations over ocean can lead to enhancement of low-level winds at night or in early morning. Zhu et al. (2020) suggested that inertial oscillations at least play a minor role in nocturnal enhancements of low-level winds and rainfall over the southern HNI. Bai et al. (2020) and Wang et al. (2021) also had similar findings near southern China coasts. The boundary layer inertial oscillation theory of Blackadar (1957) requires diurnal change in boundary layer stability and hence associated turbulence mixing, and the theory works very well over inland regions of China for early-morning rainfall peak in Meiyu front (Xue et al., 2018) and nighttime peak rainfall in Sichuan Basin (Zhang et al., 2019). The question is: what causes inertial oscillations of winds with boundary layer over ocean, where sea surface temperature does not change much diurnally as over land.

Recently, Kong et al. (2020) studied the formation mechanism of marine layer low-level jet (LLJ) over Beibu Gulf that was discussed earlier by Du and Chen (2019). They suggested that the primary source of the marine LLJ over Beibu Gulf is due to inertial oscillations over the inner plain of ICP. So far, the connection of HNI rainfall with the boundary layer flows over ICP, if present, has not been clearly identified. Determining if such a connection exists and the primary mechanism for the near-noon rainfall peak on southern HNI are the primary goals of this study.

After a climatological survey of precipitation events during the EASM seasons in HNI region using precipitation data and reanalysis data, a typical June case, which has prominent noon time rainfall peak on southern HNI (see the blue line in Figure 2), is chosen for a detailed modeling study. The rest of this paper is organized as follows. Section 2 introduces the data and methodology used. Section 3 includes a description of the rainfall event and a comparison between observation and simulation. In Section 4, processes and mechanisms associated with the diurnal cycle of marine LLJ and rainfall in southern HNI are analyzed. A summary and conclusions are given in Section 5.

2. Data and Methodology

The merged rainfall data (Shen et al., 2014) combining the satellite-estimated rainfall based on Climate Prediction Center MORPHing Technique (CMORPH) (Joyce et al., 2004) with hourly rain gauge observations over China are used to analyze the climatological diurnal cycle of rainfall on HNI and select the typical rainfall case of interest. Compared to the original CMORPH rainfall, the merged CMORPH rainfall incorporates observations from rain gauge stations and retains satellite-estimated data in areas lacking stations. Thus, the timing discrepancy existing between the CMORPH data and station observations over HNI (Zhu et al., 2017) will be effectively eliminated in the merged rainfall. Ten years (2009–2018) of hourly merged CMORPH rainfall with horizontal grid spacing of $0.1° \times 0.1°$ are used here, and the 10-year diurnal variations of precipitation climatology for June are shown in Figure 2. After a day-by-day check, the rainfall case of 19–20 June 2017 with prominent near-noon rainfall peak is chosen for detailed investigation. We note here while the 10-year mean climatology for June shows three precipitation peaks for southern HNI, days on which precipitation occurs at all three times (early morning, near noon and afternoon) are actually not common. Most times, precipitation occur at one or two times of the day. The climatological average shows the three peaks because precipitation commonly occurs near these three times.

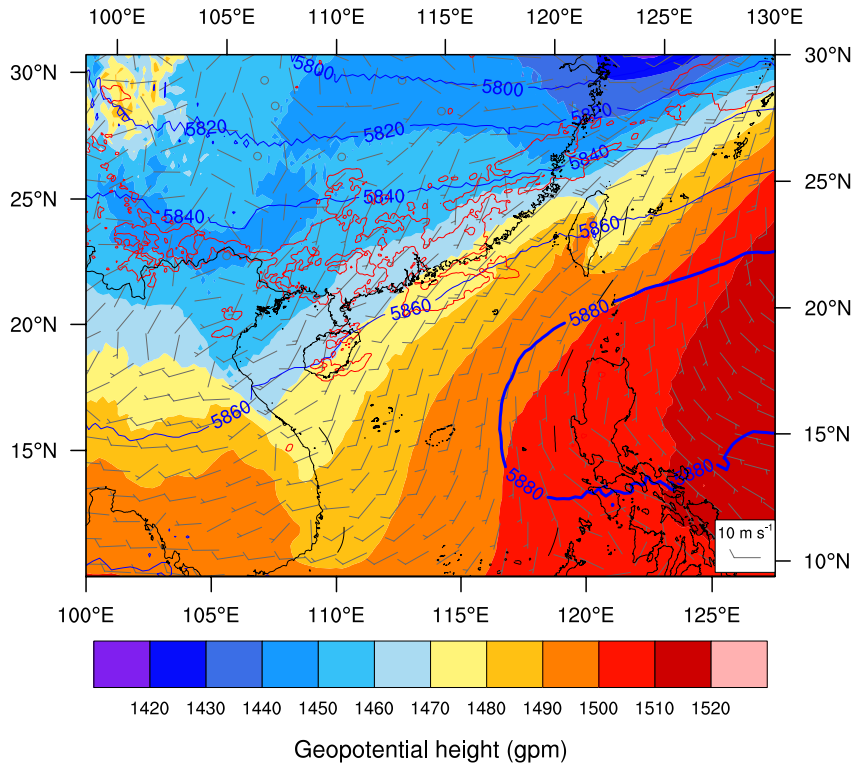

Figure 3. NCEP global model final analysis (FNL) geopotential height fields at 500 hPa (blue solid, contour interval = 20 gpm, with the line of 5,880 gpm thickened) and 850 hPa (shaded), and 925 hPa wind barbs at 08 LST 20 June 2017. The red contours represent 12 hr rainfall accumulation in excess of 10 mm from 08 LST to 20 LST 20 June 2017.

The 20 June 2017 is chosen because its near-noon peak is most prominent, and its low-level circulation pattern is close to the 10-year June average (not shown). The case is not directly affected by cold front or tropical cyclone. National Centers for Environmental Prediction (NCEP) 6-hourly Final (FNL) Operational Global Analysis data with grid spacing of 0.25° × 0.25° are utilized to depict the synoptic backgrounds prior to the rainfall event.

The Advanced Research WRF (ARW) version 3.9.1.1 (Skamarock et al., 2008), a configuration of the Weather Research and Forecasting (WRF) model, is used to carry out our simulation starting from 08 LST 19 June 2017 to 08 LST 21 June 2017. Six-hourly NCEP FNL data are used to provide initial and lateral boundary conditions for the simulation. Only one domain (Figure 1a) is used with 35 vertical levels and 601 × 601 grid points at 2 km horizontal grid spacing. To take more upstream processes into account, the center of our model (19°N, 108°E) is placed over the sea off the west coast of HNI (the open triangle in Figure 1a). Main physics options used in our simulations include the Yonsei University (YSU) planetary boundary layer scheme (Hong et al., 2006), the Thompson microphysics scheme (Thompson et al., 2008), the Rapid Radiative Transfer Model for Global Climate Models longwave and shortwave radiation schemes (Iacono et al., 2008), the unified Noah land surface model (Livneh et al., 2011), and the revised MM5 Monin–Obukhov surface-layer scheme (Jiménez et al., 2012). Most of these schemes are commonly used for simulations of mesoscale weather systems at convection-allowing resolutions. Additionally, the upper-air soundings at Sanya station (109.52°E, 18.23°N) on the southern tip of HNI (Figure 1a), together with the hourly merged CMORPH rainfall, will be used to verify the results from our simulation.

3. Diurnal Change of Convective Rainfall and Assessment of Simulation

At 08 LST 20 June 2017, the western Pacific subtropical high at 500 hPa (refer to the 5,880 gpm contour in Figure 3) appeared over the Philippines, and southwesterly winds prevailed over the ICP and the northern SCS west of the subtropical high. There existed a low-pressure center over the southern China at 850 hPa with a nearly north-south-oriented monsoonal trough along the coast of ICP. Strong southwesterly winds at 925 hPa (wind

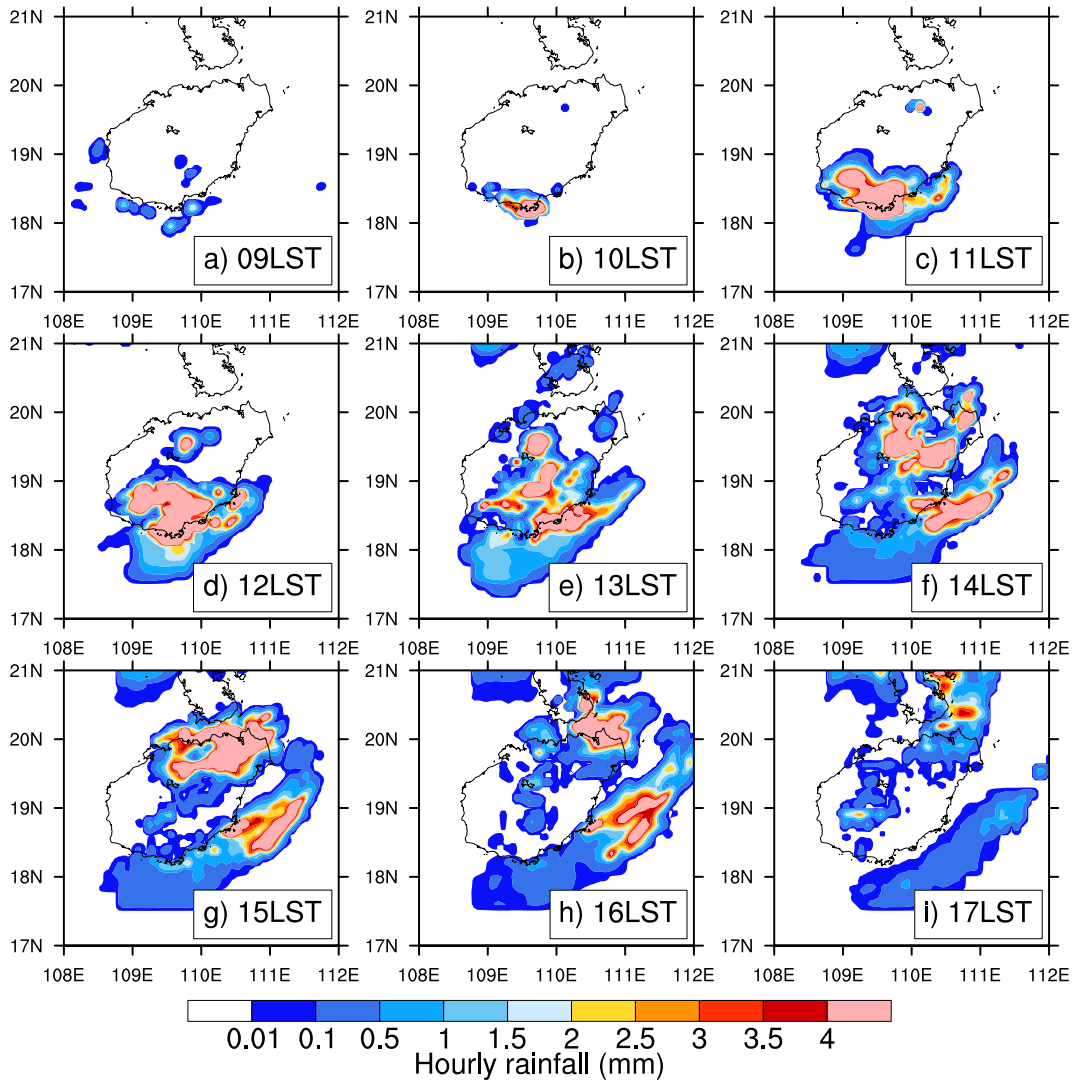

Figure 4. Observed hourly rainfall (shaded) over Hainan Island from 09 LST to 17 LST 20 June 2017 based on the merged CMORPH rainfall data.

speed ≥10 m s^{-1}) originating from the inland ICP flowed across Beibu Gulf and the strait upstream of HNI (Figure 3).

Heavy rainfall broadly occurred over the southern China mainland, and rainfall was observed not only on the windward side of HNI but also on its leeside. This rainfall case over the Island was characterized by distinct diurnal cycle with intense rainfall mostly occurring during the daytime of 20 June 2017 (Figure 4). Weak rainfall started at 09 LST off the coast of the southern HNI (Figure 4a). It intensified quickly and moved to the southern end of HNI at 10 LST (Figure 4b). From then on, the extent of rainfall on the windward side expanded rapidly and reached its peak around 12 LST (Figure 4d) while rainfall on the leeside was initiated around 11 LST (Figure 4c). Later, heavy rainfall on the windward side started to dissipate and migrated eastward. By 15 LST, the region of rainfall rate in excess of 2 mm hr^{-1} on the windward side had almost moved to the sea to the east of the Island (Figure 4g). Meanwhile, rainfall on the leeside developed quickly and reached its peak (Figure 4g). By 17 LST, rainfall in excess of 2 mm hr^{-1} on HNI almost migrated to the sea to the northeast of the Island (Figure 4i).

Figure 5 presents the WRF-simulated hourly rainfall over HNI during the same period. Some notable differences are seen between the simulations and observations. First, the modeled rainfall was initiated over the mountains and then expanded southward to the neighboring sea (Figures 5a–5d), whereas in the observations it started off and along the southern coast and then moved inland (Figures 4a–4d). Second, during the entire period of

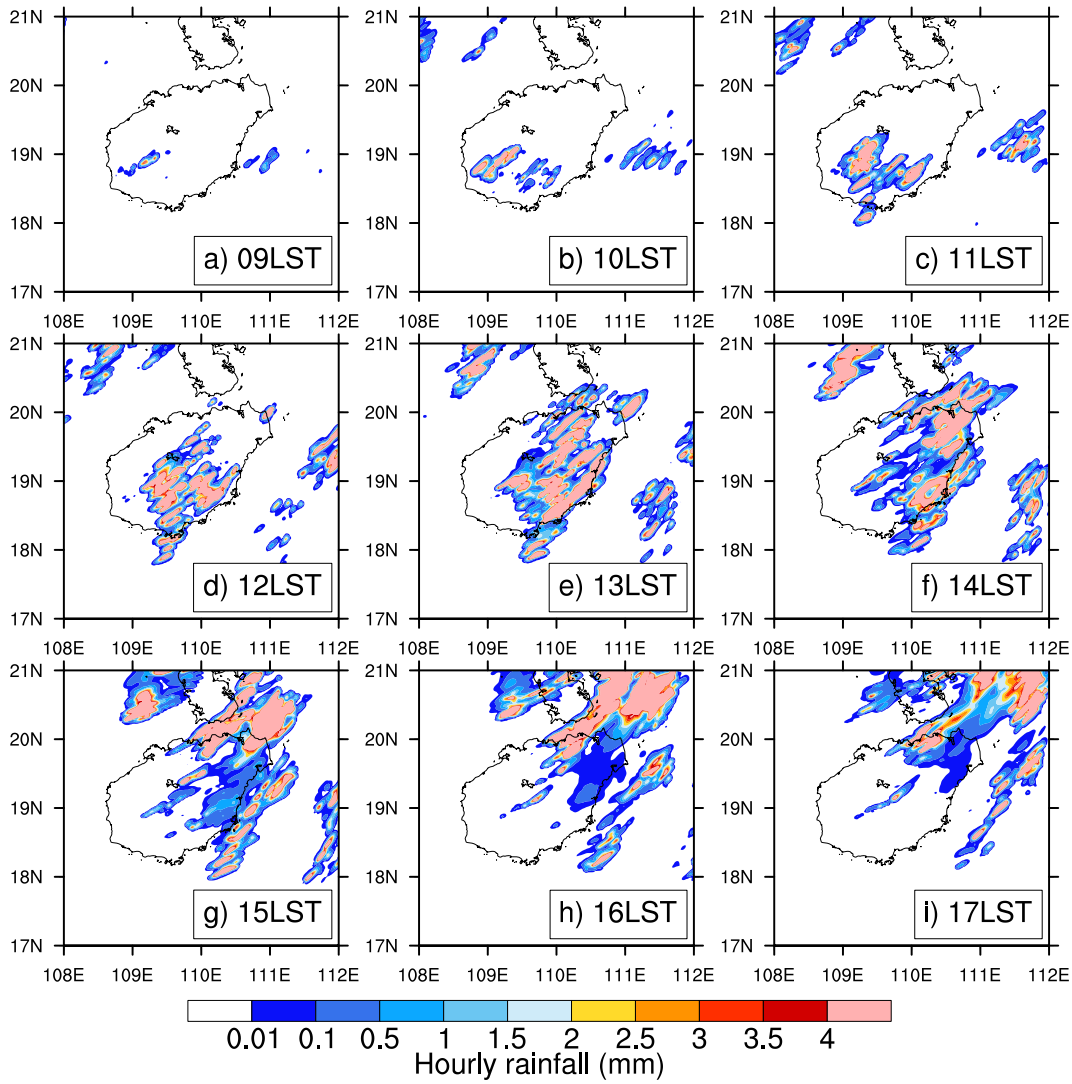

Figure 5. Same as Figure 4 but for the WRF simulation.

rainfall, the simulated extension of rainy area toward the sea off the southern coast is relatively small in comparison with the observations (cf. Figures 4 and 5d).

Despite the above discrepancies in location, the timing of model-simulated rainfall is fairly consistent with the observations (cf. Figures 4 and 5). First, the simulated rainfall peak time around 12 LST (Figure 5d) and end time at 16 LST (Figure 5h) on the windward side are consistent with the observations (Figures 4d and 4h). Second, the simulated start time of rainfall at 12 LST (Figure 5d) and peak time around 14 LST (Figure 5f) on the leeside have only 1 hr of deviation from the observations (Figures 4d and 4f). Most importantly, rainfall on both sides of the island developed independently and experienced evident separation from each other from 14 LST to 16 LST in the simulation (Figures 5f–5h) just as observed (Figures 4f–4h). Overall, the simulated evolution of rainfall on the Island agrees fairly well with the observations.

Because the focus of the present paper is on rainfall on the windward side of HNI, model-extracted sounding at Sanya station located at the southeastern corner of HNI (which is the only sounding station available in southern HNI) is compared to observed one at 08 LST 20 June 2017 (Figure 6). The simulated winds at the middle and lower levels are generally in agreement with observations, except for wind direction errors in the lowest kilometer. The wind direction error below 1 km can be attributed to timing error in diurnal wind variation at the location. The simulated winds rotate from southeasterly to southwesterly between 02 and 04 LST 20 June, earlier than real

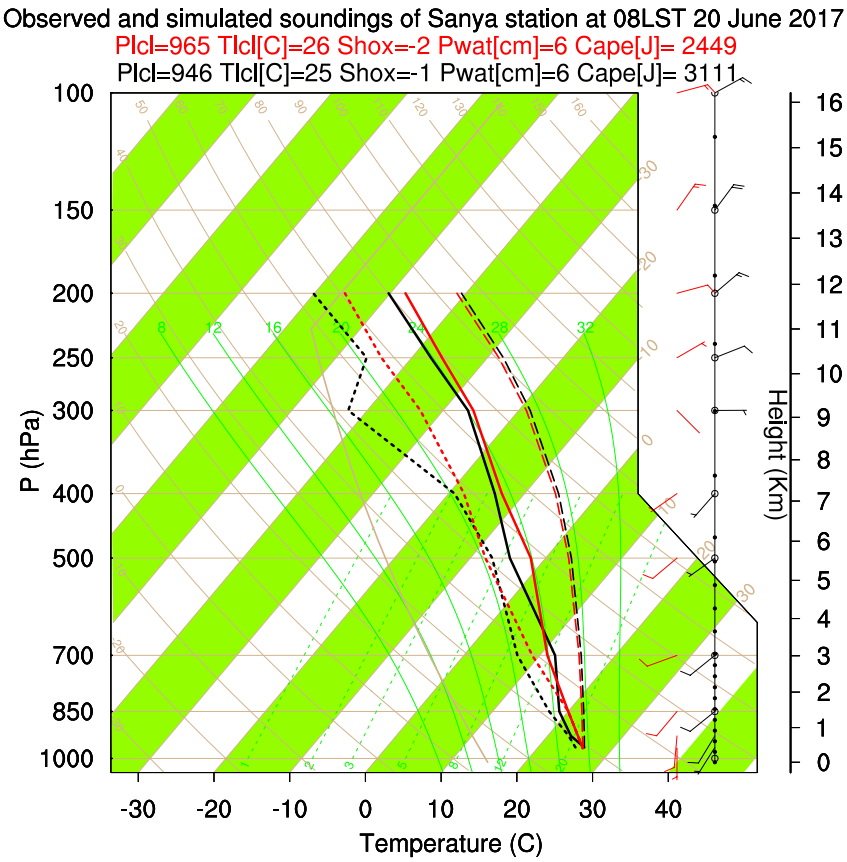

Figure 6. Comparison of observed (red) and WRF-simulated (black) soundings of Sanya station at 08 LST 20 June 2017. Dew point temperature line (dotted), temperature line (solid), and parcel line (dashed) are shown for comparison.

winds (not shown). For our problem, the wind direction and intensity along and normal to the south coast of HNI are most important. The wind direction error at Sanya station is only marginally important because it is located on the east flank of the southern coast (see Figure 1). Furthermore, the wind reversal between 300 and 400 hPa in the observation is also reproduced correctly by simulation.

For temperature and dew point temperature, although our simulation is a little colder below 2 km and above 4 km, and moderately drier below 4 km and above 6 km than the observations, the simulated thermodynamic attributes of the atmosphere near the surface are generally in agreement with the observations (Figure 6). For instance, the simulated convective available potential energy (CAPE) of 3,111 J kg^{-1} is just a little larger than the observed value of 2,449 J kg^{-1}. Given the fact that CAPE is sensitive to errors in moisture and temperature near the surface and temperature profile at upper levels, such a difference in CAPE is considered acceptable. To sum up, our simulation is able to reproduce not only the diurnal cycle of rainfall on both sides of HNI but the winds and thermodynamic stratification on the southern Island. Hence, it can be used to analyze the mechanisms underlying the diurnal cycle of rainfall on the southern HNI in our case.

4. Mechanisms of Diurnal Changes of Convective Rainfall

4.1. Impact of Boundary Layer Inertial Oscillations on Convective Rainfall Peak Around Noon

4.1.1. Diurnal Variations of Boundary Layer Winds

Diurnal variations of low-level winds over the southern HNI in our case bear a strong resemblance to boundary layer inertial oscillations except for a significant time delay (Figure 7). In the region enclosed by the blue rectangle in Figure 7a, an obvious clockwise rotation of wind direction is observed at 925 hPa in our simulation. That is, the wind direction starts from southerly at 02 LST, then turns into southwesterly at 06 LST and 10 LST, and ends

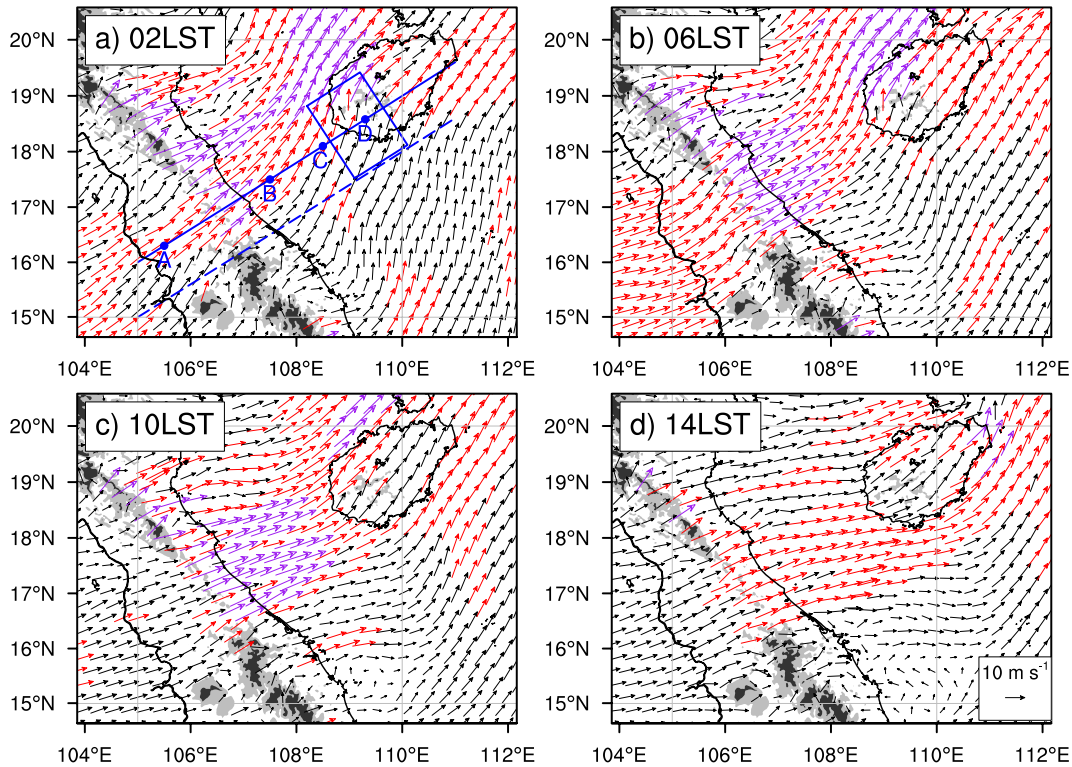

Figure 7. WRF-simulated 925 hPa wind fields, at (a) 02 LST, (b) 06 LST, (c) 10 LST, (d) 14 LST on 20 June 2017. Terrains higher than 700 and 1,200 m are shaded with gray and dark gray, respectively. Vectors shaded with red and purple designate wind speed larger than 10 and 15 m s^{-1}, respectively. Vertical cross sections will later be performed along the blue solid and dashed lines. Points A, B, C, and D indicate the locations where diurnal cycles of wind are examined. The blue rectangle marks the region where water vapor flux is computed in Figure 13.

up being westerly at 14 LST (Figures 7a–7d). This clockwise rotation of wind vectors can be more clearly seen from Figure 8 in which hodograph plots of 925 hPa winds at points A, B, C, and D (see Figure 7a) are shown. To reduce localized noise, wind vectors are obtained by averaging over squared regions of 40 × 40 km centered at the corresponding points. C and D are situated offshore and onshore near the windward HNI, respectively. Despite some deviations around midnight, there exists a clear feature of boundary layer inertial oscillations in wind vectors of these two points (Figures 8c and 8d). From 10 LST through 14 LST when the wind speeds are strongest over southern HNI and the neighboring sea (Figures 7c, 7d, 8c, and 8d), the intensity of rainfall over there reaches its peak (Figures 5b–5f). It is therefore reasonable to believe that the diurnal change of rainfall on the windward side of HNI is closely related to the enhancement of the low-level onshore winds and the associated lifting by the coastal mountains, as was also proposed by earlier studies on south China coastal rainfall (Chen et al., 2015; Du & Chen, 2019; Du et al., 2020; Li et al., 2019). The question is: given that the onshore flows come from the ocean, why do they undergo diurnal changes similar to the inertial oscillations in boundary layer over land? At the same time, why is the peak speed of the wind reached near the Island at around 11 LST rather than in early morning? Because the low-level ambient flow is southwesterly, we try to trace back along the flow toward the upstream all the way to the coast of ICP, along the solid blue line in Figure 7a. Interestingly, the low-level wind direction off the shore of ICP (Point B) exhibits similar diurnal changes as those near HNI but the wind speed peaks at around 09 LST, 2 hr earlier than the 11 LST of HNI, and then it weakens significantly by 14 LST (Figure 8b).

Tracking along the blue line further upstream to the inland plain of ICP where the Blackadar boundary layer inertial oscillation theory can fully operate, the wind vectors at A in Figure 7a also experience clockwise rotation (see also Figure 8a) but the wind speed peaks much earlier at around 06 LST (Figure 8b and bottom-left corner of Figure 7b), a time much more consistent with the prediction of Blackadar's theory. Thus, based on the above facts, we can preliminarily infer that the source of wind rotation on the windward side of HNI, which is most likely to be responsible for the diurnal change of rainfall there, originates from the boundary layer over the inland plain of ICP, and the oscillating winds are advected downstream to the ocean where surface friction is reduced.

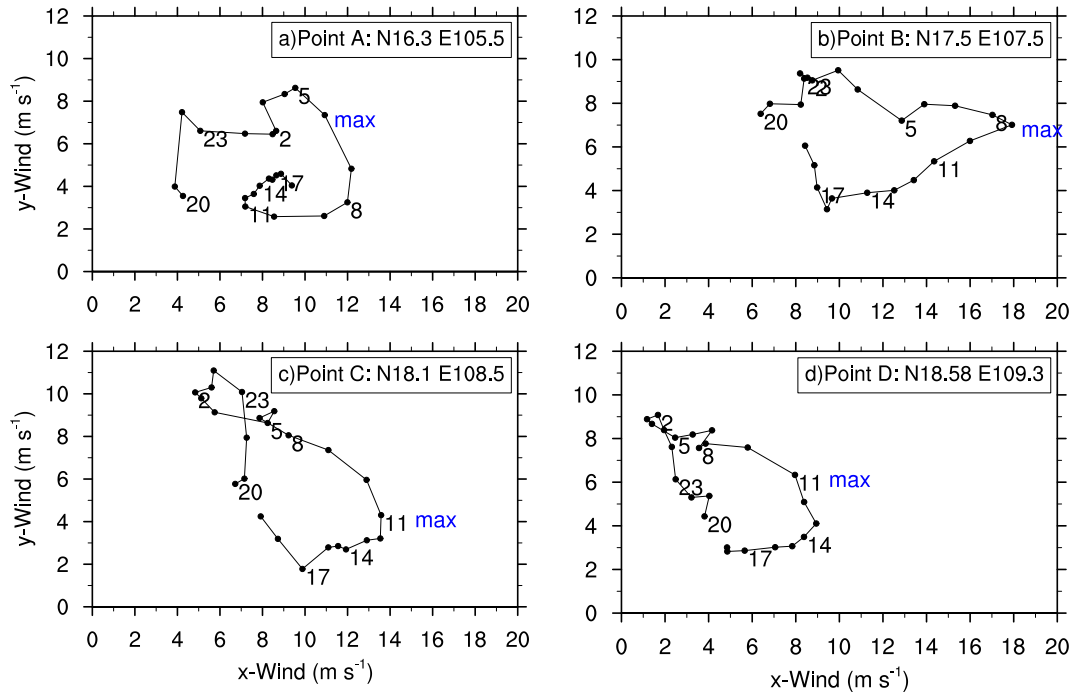

Figure 8. Area-averaged 925 hPa wind vectors from 20 LST 19 June through 19 LST 20 June over squares of 40 × 40 km with centers at points A (a), B (b), C (c), and D (d) in Figure 7a, respectively. Dots on the curves and numbers beside the dots indicate the tips of wind vectors from the coordinate origin and the corresponding local times, respectively. Label "max" indicates the time when the wind speed peaks.

Given the time needed for the signal to travel over the ocean channel, the time that peak wind speed occurs at the Island is delayed by about 5 hr.

To verify our thesis proposed above, vertical cross sections of wind and potential temperature along the blue solid line in Figure 7a are plotted in Figure 9. The winds between 500 and 800 m above ground level (AGL) over the inland plain of ICP are found to increase from 4 to 6 m s^{-1} at 20 LST 19 June (not shown) to 12–14 m s^{-1} at 06 LST 20 June (Figure 9b) due to decoupling of the boundary layer from the lower surface layer at night. As a result, a boundary layer LLJ forms. After traversing the low coastal hills of the gap, the LLJ flows accelerate downslope, reaching speed of 18–23 m s^{-1} in the 400–900 m AGL layer at 06 LST on the ocean side (Figure 9b). Meanwhile, compared to 02 LST, the wind speed over the sea has increased drastically and the leading edge of LLJ below 1 km, as defined by the 12 m s^{-1} contour, is approaching the windward side of HNI by 06 LST (Figure 9b). The ≥15 m s^{-1} LLJ has reached the middle of the strait. By 10 LST, the winds over ICP weaken significantly as daytime boundary mixing develops while on the ocean side of the mountain range the region of 15–18 m s^{-1} LLJ extends downstream to reach about 3/4 of the width of the strait. The ≥18 m s^{-1} LLJ core has shifted from the ICP lee slope at 06 LST to reach the middle of the strait (Figure 9c). This leads to the peak onshore wind speed near HNI at ~11 LST, as noted earlier. At 14 LST, apparently due to lack of continuous supply of positively enhanced flow from upstream (actually negatively perturbed winds would be arriving), the winds over the coastal hills of the Peninsula weaken significantly, and the LLJ over the downstream sea has only a small core of about 12 m s^{-1} winds (Figure 9d).

The simulated upward motion near the southern coast of HNI is much more notable from 06 LST to 10 LST (Figures 9b and 9c) than at other times. This agrees with our earlier inference that the terrain lifting of enhanced winds on the windward side of HNI is the direct cause of convection initiation in daytime in this case. Although rainfall occurs mostly from 10 LST and 14 LST on southern HNI, the earlier process of destabilization is indispensable and the convective systems need some time to reach maturity after initiation. At 14 LST (Figure 9d), there is an upward bulge of potential temperature contours offshore of the HNI, clearly due to upward lifting there, while onshore near the island coast the contours turn vertical, a result of vertical convection.

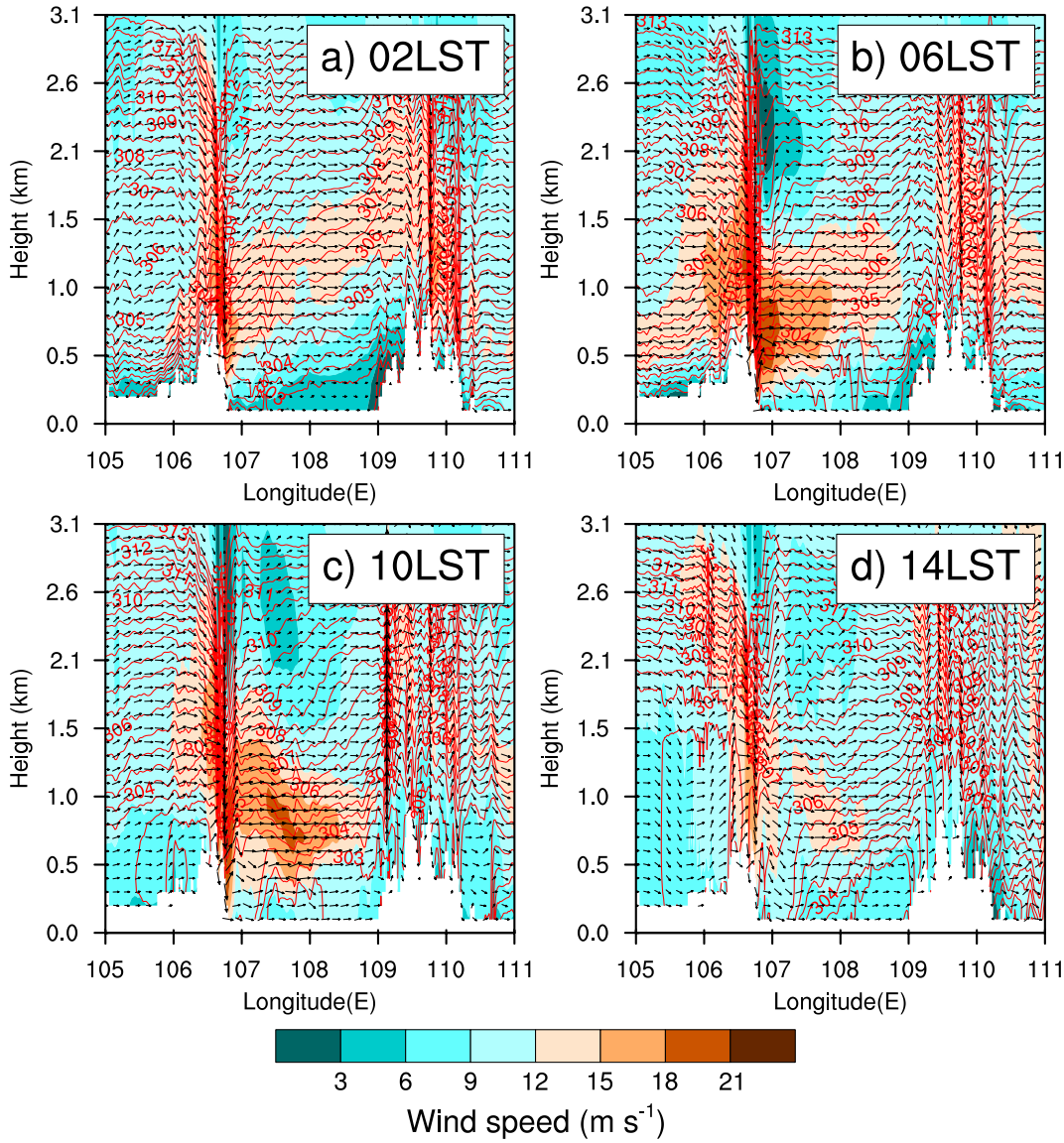

Figure 9. Vertical cross sections for wind vector, wind speed (shaded), and potential temperature (contours, interval = 0.5 K) along the blue solid line in Figure 7a at (a) 02 LST, (b) 06 LST, (c) 10 LST, (d) 14 LST on 20 June 2017. Wind vectors contain vertical component amplified by a factor of 10 and horizontal component parallel to the blue solid line. Wind speed is the real magnitude of wind vectors in the plane.

4.1.2. Effects of a Gap in the Coastal Mountain Range of ICP and the Associated Downslope Winds

As pointed out earlier, an orographic gap or channel with altitude mostly lower than 700 m exists in the coastal Annamite Mountain range, just upstream of HNI (see Figures 1a and 7). Over the mountain range, especially through the gap, wind speed is generally larger than that over the lower plains of ICP throughout the day. Moreover, the oceanic region with highest wind speed and most clear diurnal change is mainly located downstream of the gap. Obviously, the presence of the gap has a channeling effect. In an idealized case of a long narrow gap between limited-size terrains discussed by Gaberšek and Durran (2004), airflows can bypass the gap on the flanks of the terrains. Unlike the idealized case, the short wide coastal gap in our case seems to be the only gateway to the sea for the low-level winds on the inland plain. The wind intensity within the gap would be amplified notably compared to those over the plain. As can be seen from Figure 7, both in nighttime and daytime, low-level airflows on the plain push their ways preferentially through the gap to the sea. Consequently, the flows reaching the downstream HNI are relatively strong, and they carry the inertial oscillation signals originating from the plain of ICP.

Apart from the channeling effect of the gap, another phenomenon worthy of noting is that significant acceleration of winds and a hydraulic jump can be seen on the leeward slope of coastal mountains of ICP at 06 LST (Figure 9b). Such processes can cause downslope windstorms in extreme cases (Durran, 1986) and have also been observed by Kong et al. (2020). According to Figure 9, the typical altitude difference between the inland plain and the coastal hills within the gap is about 500 m. Assuming a Brunt-Vaisala frequency at night of 0.01 s^{-1} and using 1.0 as the threshold Froude number, a speed of only 5 m s^{-1} is sufficient for the near surface layer flow to pass over the hills. With the help of nighttime LLJ acceleration, this criterion is easy to meet. On the other hand, the airflows near the surface have been radiatively cooled at night. Once they pass over the low hills, they can accelerate downslope and form a hydraulic jump (Durran, 1986). However, it is not the case in areas outside the gap where the mountain range is much higher. Along the blue dashed line in Figure 7a, with a plain-mountain elevation difference of more than 1,000 m, the flows that can climb over the mountain are mostly from the more elevated layers with higher potential temperature. After the airflows pass over the mountain, the resulting descent and acceleration is much weaker than those over the gap (not shown). As a result, with the further help of downslope winds developing in the lee of the coastal mountain over the gap, the inland oscillating winds in a LLJ core are advected toward the downstream sea and HNI at a faster speed and with a larger amplitude, especially off the shore of ICP in the morning (Figure 8b).

4.1.3. Clockwise Rotation of LLJ Wind Vectors Across the ICP-HNI Strait and Its Cause

As already revealed in Figure 8, clockwise rotation of wind vectors has been observed at various locations over the ICP-HNI strait like B, C and D. To be sure that the clockwise rotation is the result of unbalanced ageostrophic winds undergoing inertial oscillations, ageostrophic winds are obtained by subtracting geostrophic winds calculated from geopotential fields filtered by a low-pass Barnes filter following Xue et al. (2018). With the filtering, wavelengths shorter than 500 km will be mostly removed. Figure 10 shows the diurnal cycles of ageostrophic and geostrophic winds for points A, B, C, and D. These vectors are averaged over 40 × 40 km boxes as before. The amplitudes of diurnal change of geostrophic winds at all four points are much smaller than those of ageostrophic winds, especially at B, C and D. At A, the ageostrophic wind has the smallest (largest) southwesterly component at 20 (06) LST while the geostrophic wind shows directional swings but little change in speed (Figure 10a). The diurnal change of geostrophic wind at A, that is, the increase of northwesterly wind at night and the enhancement of southeasterly wind in daytime, can be explained by thermal wind over sloping terrain that was proposed by Holton (1967) as an alternative mechanism for diurnal variation of boundary layer winds. According to the theory, during daytime on the west side of Annamite range as the heating over the mountain range sets up positive temperature gradient toward the mountain range, the thermal wind should be southeasterly while at night thermal wind reveres direction so it is northwesterly. The thermal wind causes changes in geostrophic winds that are consistent with those shown in Figure 10a, which are nearly parallel to the mountain range of ICP. However, given that such perturbation geostrophic wind vectors are mostly perpendicular to the path toward HNI (or the blue thick line in Figure 7a) and hence parallel to the southern coastline of HNI, the contribution to the enhancement of coastal precipitation is expected to be limited, even if the perturbations are advected toward and arrive at the HNI coast. Regarding the afternoon deviation of ageostrophic wind at A from the typical clockwise rotation (Figure 8a), as noticed previously, local terrain or convection might have caused it. The diurnal cycles of ageostrophic winds at B, C, and D exhibit more clearly defined clockwise rotation than those of total winds. At B, the much larger enhancement of southwesterly flows in the morning hours is linked to the leeside acceleration discussed earlier (see Figure 9c). According to Figure 10, the peak southwesterly ageostrophic wind speed is reached at 06, 09, 11, and 11 LST for A, B, C, and D, respectively, consistent with the downstream advection (ADVEC) of oscillation signals.

To further confirm the mechanism of diurnal changes, terms in Equation 1, for momentum at 925 hPa are calculated for the 40 × 40 km regions centered at the four locations. The diagnostic calculations are similar to those used in Fu et al. (2019), Kong et al. (2020) and Du et al. (2020).

$$\underbrace{\frac{\partial u}{\partial t}}_{\text{TEND}} = \underbrace{\left(-u\frac{\partial u}{\partial x} - v\frac{\partial u}{\partial y}\right)}_{\text{ADVEC}} \underbrace{- w\frac{\partial u}{\partial p}}_{\text{VERT}} \underbrace{+ f\,(v_g - v)}_{\text{CORI}} \underbrace{+ F}_{\text{RESID}} \tag{1}$$

In Equation 1, u is the wind component projected to the blue solid line in Figure 7a and v the component perpendicular to u. The term on the left-hand side of Equation 1 is the local time tendency of u (TEND) and those

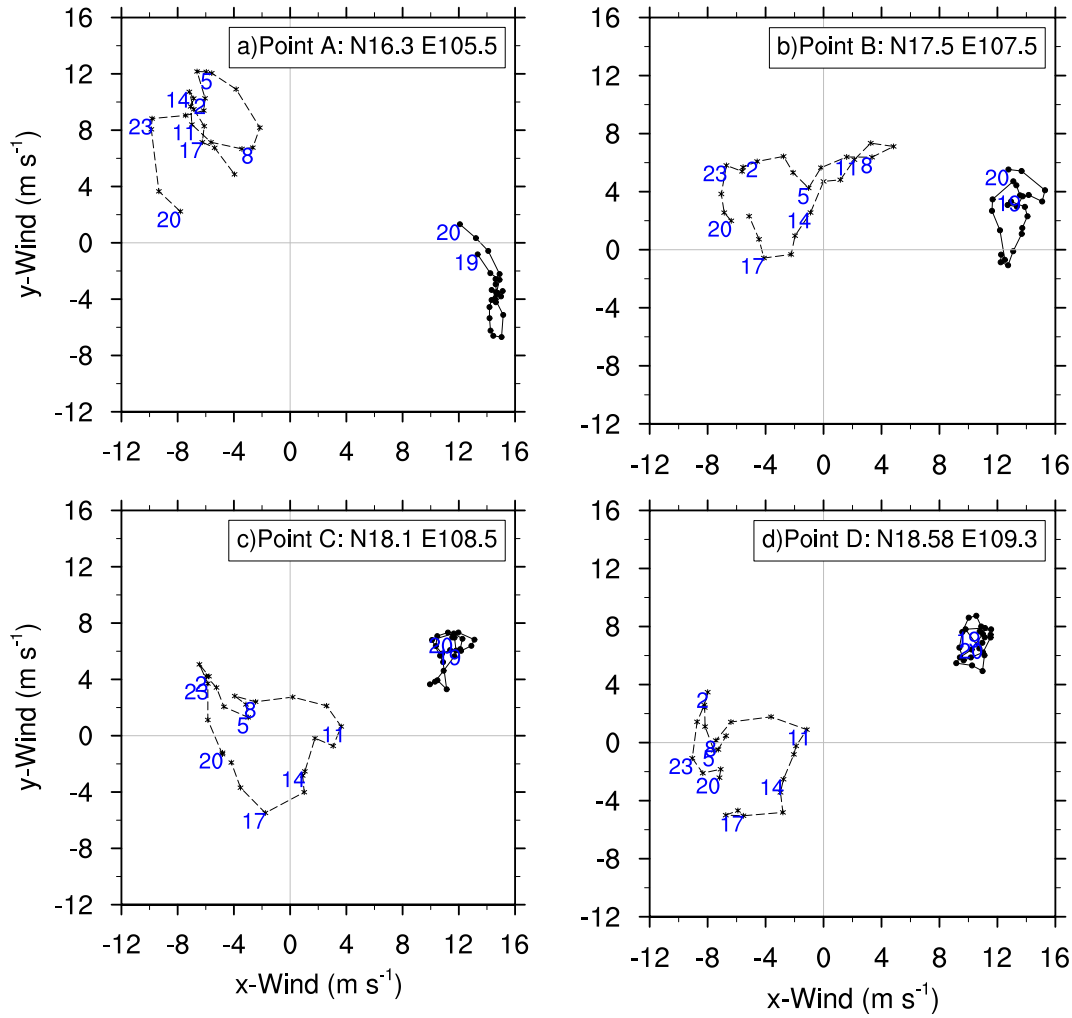

Figure 10. Area-averaged 925 hPa ageostrophic (dashed curves with asterisks) and geostrophic (solid curves with dots) winds from 20 LST 19 June through 19 LST 20 June over squares of 40 × 40 km centered at points A (a), B (b), C (c), and D (d) in Figure 7a. Dots and asterisks on the curves and numbers beside them indicate the tips of wind vectors from the coordinate origin and the corresponding local times, respectively.

on the right-hand side are horizontal advection (ADVEC), vertical advection (VERT), Coriolis term acting on ageostrophic winds (CORI), and residual term related to turbulence mixing, etc. RESID. From Figure 11a, the other terms on the right-hand side of Equation 1 at A are relatively small compared to CORI before 06 LST with a brief increase in ADVEC around 04 LST being largely canceled out by RESID. Thus, wind acceleration at A before 06 LST is mostly due to unbalanced Coriolis force, consistent with the inertial oscillation theory. It can also be seen that TEND becomes zero at 06 LST (Figure 11a) when the wind speed peaks (Figure 8a). After 06 LST, the residual term RESID related to turbulence mixing tends to be large and negative with sunrise when boundary layer mixing develops in response to surface heating and the jet core in the vertical wind profile is still well defined (Figure 11a). Correspondingly, TEND turns large and negative also. As a result, the wind speed at A decreases sharply. In the afternoon when jet is mixed out, RESID becomes smaller. The time series pattern shown in Figure 11a is similar to that of Figure 8 of Fu et al. (2019) who found diurnal oscillations of upstream boundary layer winds to be the primary reason for nighttime precipitation peak over Dabie Mountains, China.

In contrast to A, horizontal advection term ADVEC at B prevails over the Coriolis term from 00 LST on, especially in the late morning. Furthermore, TEND at B is almost in phase with ADVEC (Figure 11b) and both decrease to zero at 08–09 LST, apparently due to the passing of peak LLJ speed through the location. The RESID is also large but negative before 08 LST, which should be related to turbulent motion to the lee of the coastal ridge which acts to slow down some of the downslope acceleration. In general, diurnal change of winds at B is

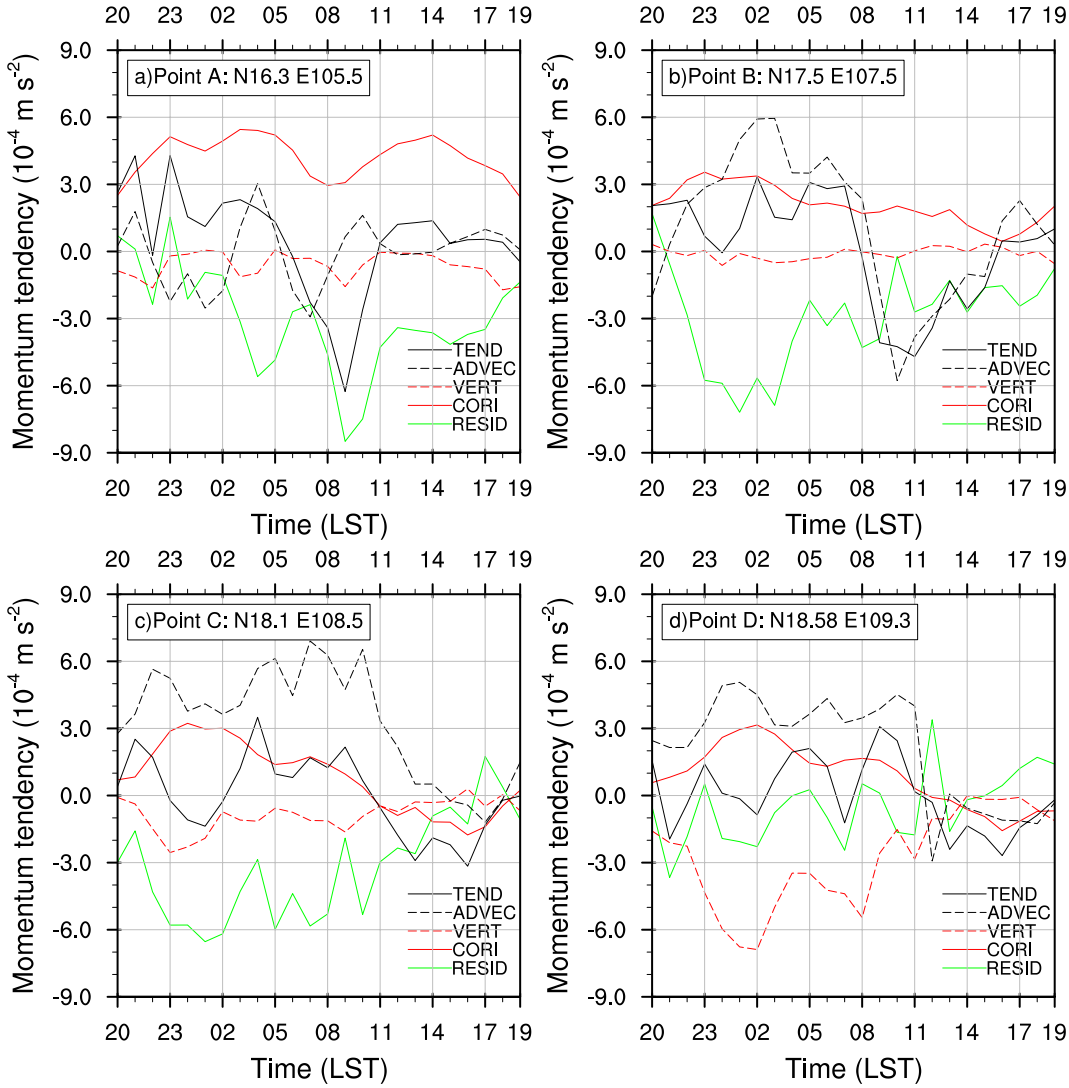

Figure 11. Area-averaged 925 hPa diurnal variations of local time tendency (TEND), horizontal advection (ADVEC), vertical advection (VERT), the Coriolis term related to ageostrophic wind (CORI), the residual term associated with turbulence mixing, etc. (RESID) for the momentum component in the direction of the blue solid line in Figure 7a over squares of 40 × 40 km centered at points A (a), B (b), C (c), and D (d), respectively. The abscissas represent times from 20 LST 19 June through 19 LST 20 June.

dominated by horizontal advection from the upstream. The relative behaviors of the terms at C are similar to those at B, but with significant delay in phase. ADVEC remains large and positive until 10 LST and does not turn negative until 15 LST (Figure 11c). Both CORI and TEND turn negative at 10 LST, and vertical advection becomes non-negligible at this point, especially in earlier hours. The rising motion is removing some of the momentum brought in by horizontal advection. RESID sink term is also large early on as at B, suggesting turbulence has not fully settled down by this point. At D, ADVEC remains the largest positive term before 11 LST, which is followed by CORI. RESID becomes much smaller but the negative vertical advection term becomes much larger and is the largest sink (Figure 11d). The much stronger vertical motion associated with the coastal orographic lifting is removing a lot of the horizontal momentum advected in. At 11 LST, much change occurs when the total time tendency TEND turns negative and all terms become relatively small. This should be due to the breakout of convection at this onshore location, and vertical motion starts to take over. To sum up, the above analyses of momentum equation further prove that most of the diurnal changes of boundary layer flows over the sea upstream of HNI originate from the boundary layer inertial oscillations over the inland ICP, and the associated ageostrophic

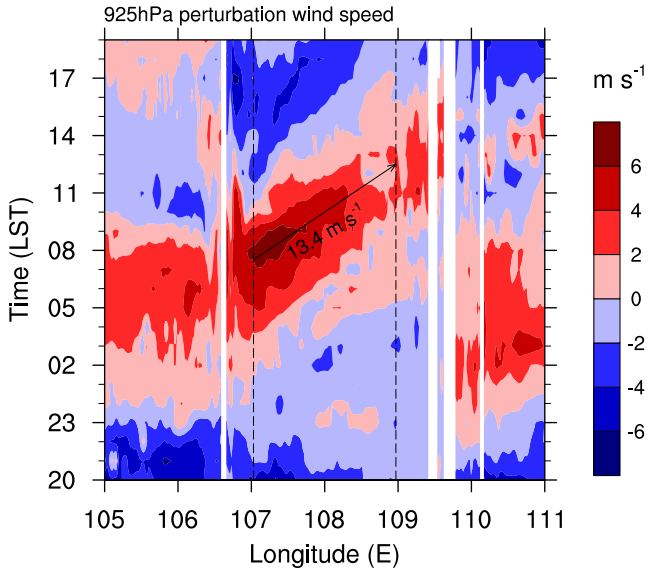

Figure 12. Hovmueller diagram of 925 hPa *u* wind perturbation from the daily mean in the direction of the blue solid line in Figure 7a. The ordinate represents times from 20 LST 19 June through 19 LST 20 June. The left and right dashed lines denote the coastlines of Indochina Peninsula and Hainan Island, respectively. The slant long black arrow and the number below indicates the estimated propagation speed of the layer low-level jet core.

winds are then transported downstream by the southwesterly flows across the strait and the peak wind speed eventually reaches southern HNI near local noon.

4.1.4. Hovmueller Diagram Depiction of Downstream Propagation of Inertial-Oscillation-Induced LLJ Core

The strong horizontal advection effect over the sea can be more clearly seen in a Hovmueller diagram of 925 hPa *u* wind perturbation from the daily mean (Figure 12). According to the diagram, periodic acceleration and deceleration appear over the inland plain of ICP without east-west propagation, which is in line with locally generated oscillations. Consistent with Figure 10a, the perturbation wind speed peaks at around 06 LST over the plain and 07 LST on the coast of ICP. Periodic variations are also evident over the sea but with an obvious trend of downstream propagation. Based on Figure 12, the time for the LLJ core to reach HNI from the coast of ICP is about 5 hr, that is, from 07 LST to 12 LST. Given that the distance between the coastlines is ~240 km, the speed of propagation is estimated to be 13.4 m s^{-1}, which is a little slower than the average wind speed of 15 m s^{-1} over the sea during the same period. After 09 LST, negative perturbation winds first appear over the inland plain and then near the coastline of ICP. Apparently, it is due to the retarding effect of daytime boundary layer mixing. The LLJ then weakens rapidly. The negative perturbation winds are transported downstream although at a somewhat lower speed (indicated by steeper slope of the blue axis in Figure 12). By 14 LST, the negative perturbation winds have advanced to the sea off the coast of southern HNI. The negative perturbation winds would decrease onshore wind speed and induce downward motion near the coast as part of an oscillating vertical circulation in the strait, suppressing precipitation in afternoon hours. This will be discussed further in Section 4.2. Overall, the LLJ core is basically a region of enhanced momentum whose propagation is due to advection, so it is the speed of the environmental wind plus the speed of perturbation wind that determine the speed of downstream propagation of the LLJ core.

4.1.5. Moisture Flux Convergence Into Southern HNI

To show how the onshore flow speed changes actually affect precipitation in southern HNI, a low-level moisture flux budget analysis is performed. A region enclosed by the blue box in Figure 7a with the top at 2 km mean sea level (MSL) is chosen to calculate water vapor flux through the four border planes and the net water vapor flux into the box (Figure 13). According to Figures 4 and 5, this region is where most of the rainfall in southern HNI occurs. Based on Figure 13, the southwest plane is the primary source of water vapor owing to the southwesterly prevailing winds. The water vapor flux through this plane has a primary peak around 10 LST and a secondary peak around 01 LST, largely reflecting the diurnal change of wind strength. The secondary source of water vapor originates from the southeast plane mainly from late night to 10 LST, and its diurnal changes are also associated with wind changes through that plane (see Figure 7). The flux through the northeast and northwest planes are mostly negative, reflecting the direction of prevailing winds. The net flux into the box has two maxima 23 LST 19 June and 10 LST 20 June, occurring at about the same time when the southwest plane flux peaks. Although the prior maximum of 23 LST is somewhat larger, the absence of rainfall can be explained by the level of free convection (LFC) higher than 2000 m MSL around 23 LST. From 23 LST through 09 LST, the LFC decreases sharply to 600 m, presumably due to the forced lifting of airflows as they approach the coast (see Figure 9). Rainfall starts at 06 LST on southern HNI, then enhances abruptly at 09 LST and reaches its peak at 12 LST. To sum up, the enhanced LLJ in the morning hours on the one hand transports ample water vapor to the southern HNI, and on the other, it forces modest and continuous upward motion and causes destabilization and decline of LFC there. When the conditions of water vapor, destabilization and lifting are all met at once, convective rainfall can occur.

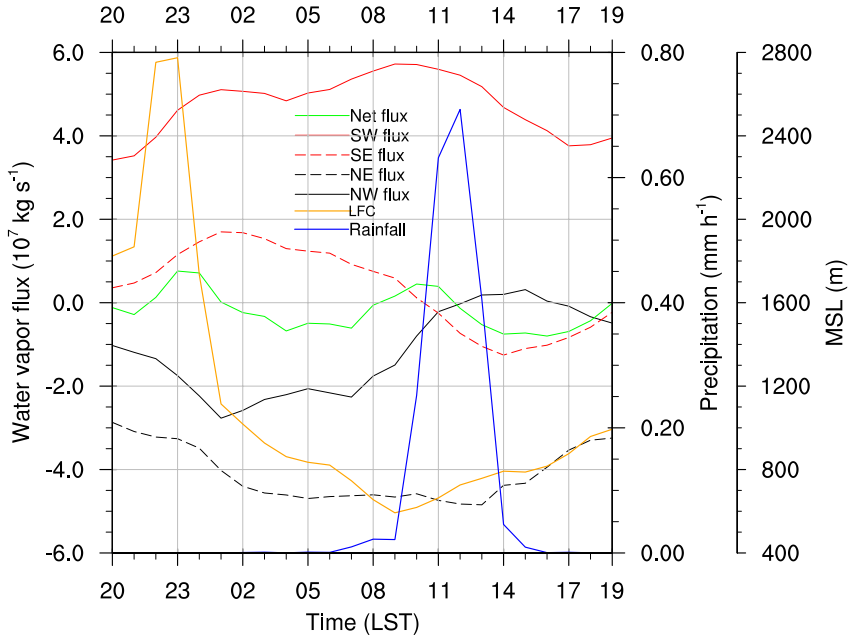

Figure 13. Diurnal cycles of water vapor flux below 2 km MSL through the southwest (SW), southeast (SE), northeast (NE), and northwest (NW) planes of the blue box of Figure 7a, and the net flux in the box (Net). Positive and negative flux is perpendicular to the corresponding plane and directed inside and outside the box, respectively. Area-averaged hourly rainfall and level of free convection (LFC) over the box are also shown. The abscissa represents times from 20 LST 19 June through 19 LST 20 June.

4.2. Impact of Boundary Layer Inertial Oscillations on Rainfall Dissipation in the Afternoon

Figure 13 shows that the rainfall on the southern HNI weakens rapidly after 12 LST and then completely dissipates around 16 LST. Vertical cross sections of perturbation wind vectors from the daily mean along the blue solid line in Figure 7a are shown in Figure 14 to reveal the relationship between the weakened LLJ and the weakening of vertical motion on southern HNI. Compared to 12 LST (Figure 14b), only a remnant of positive horizontal perturbation winds remains on southern HNI by 15 LST (Figure 14c). As a result, the ascent on the windward slope of southern HNI mountains weakens significantly and rainfall weakens accordingly. By 18 LST, the coastal region is completely occupied by negative perturbation winds (Figure 14d). Based on Figures 11c and 11d, the horizontal momentum advection term, which is dominant during night and in the morning, turns from positive into negative in the afternoon, suggesting that downstream advection of wind perturbations causes diurnal flow changes at southern HNI.

Upstream of HNI over the inland plain of ICP, negative perturbation winds in the boundary layer first appear around 500 m MSL at 09 LST (Figure 14a). They extend upward to 1.5 km MSL as well as eastward to the coast of ICP by 12 LST (Figure 14b). Those over the inland plain should be mainly due to vertical mixing related to solar insolation, which is confirmed by the almost uniform potential temperature below 1.5 km MSL in that region (Figure 14b). An uncertainty lies in whether the negative winds over the coast of ICP are mainly due to vertical mixing or due to sea breeze. There are at least two evidences supporting vertical mixing as the main contributor. The first is that negative perturbation winds are higher up while positive perturbation winds are close to the ground (Figures 14a–14d). It is similar to the case on the inland plain where vertical mixing dominates and sea breeze is unlikely to have an influence. The second evidence is that the 10 m offshore winds near the coast of ICP range from 6 to 8 m s^{-1} between 08 LST and 14 LST (not shown). According to Crosman and Horel (2010), sea breeze will be absent when offshore wind strength ranges from 6 to 11 m s^{-1} near the coastline. It can be seen from Figure 14b that owing to strong environmental winds, the zone with strong horizontal temperature gradient is largely located over the sea off the coastline of ICP rather than just near the coastline. Thus, sea breeze cannot develop near the coastline, let alone advance onshore.

The zone of negative perturbation winds over the coast first seen at 12 LST continues to develop and expand seaward by 15 LST, while a narrow zone of thermally induced upslope winds appears on the coastal mountain

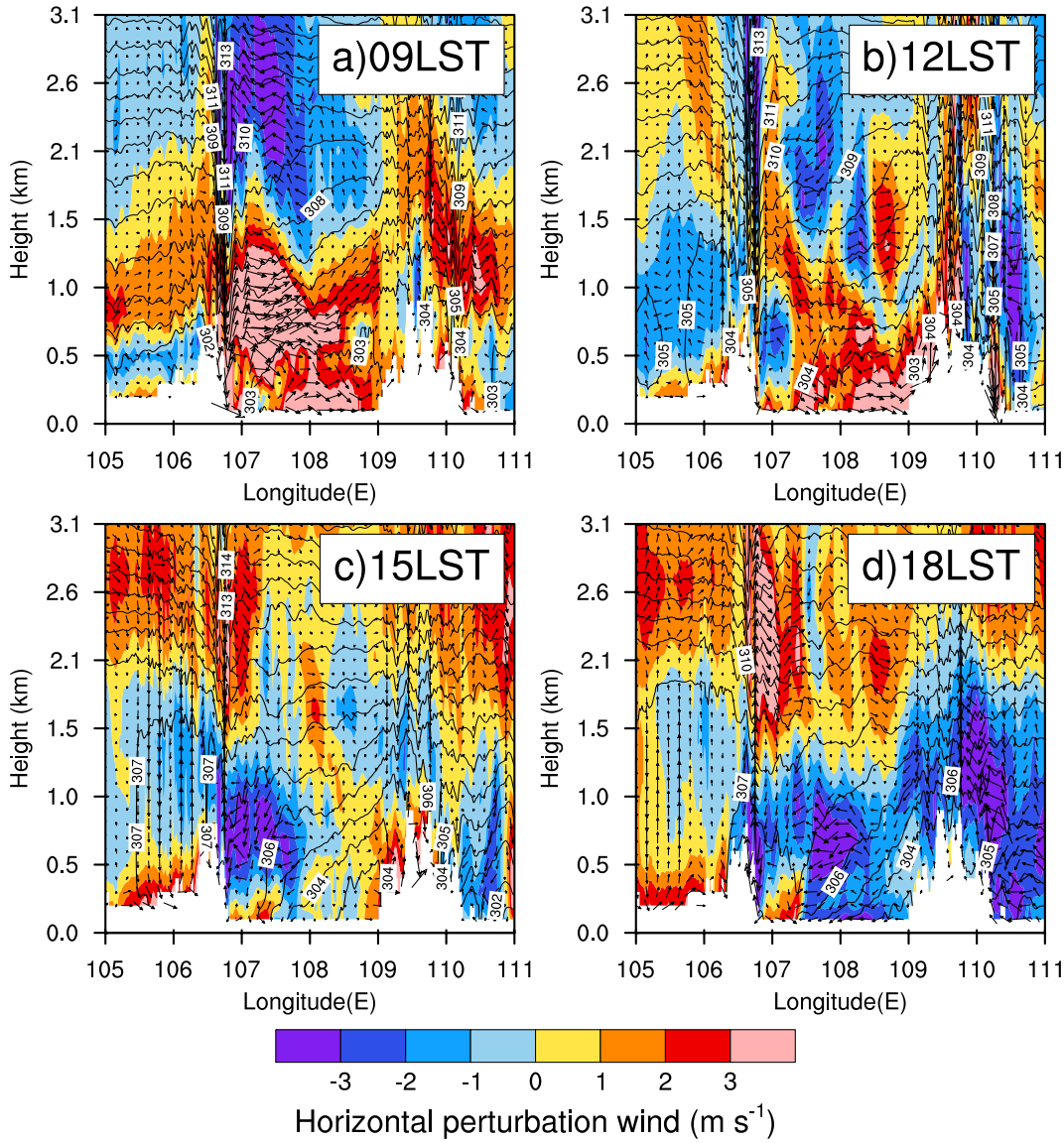

Figure 14. Vertical cross sections of potential temperature (contour, interval = 1 K), perturbation wind vector (with vertical component amplified by a factor of 10), and horizontal perturbation wind (shaded) along the blue solid line in Figure 7a at (a) 09 LST, (b) 12 LST, (c) 15 LST, (d) 18 LST on 20 June 2017.

slopes of ICP (Figures 14b and 14c). At 18 LST, the zone of strong negative perturbation winds advances farther to 109°E, replacing positive perturbation winds at the coast of HNI while upslope winds remain on the ICP mountain slope (Figure 14d). Meanwhile, obvious descent is induced below 1.5 km MSL on the windward slope of the mountains of HNI by the negative low-level perturbation winds (Figure 14d). The descent causes boundary layer stabilization as evidenced by the lowering of, for example, the 306 K potential temperature contour (Figures 14c and 14d), and rainfall over the southern island is therefore suppressed. The stabilization is further confirmed by examining both simulated soundings and the terms in the potential temperature equation at point D: the air ranging from 1.5 to 2.0 km MSL warms up notably after 14 LST due to the dominant positive vertical advection term, whereas the air temperature below remains almost constant owing to the diabatic heating largely offset by the cooling related to the horizontal advection term (not shown).

To sum up, on one hand, the terrain-forced upward motion decreases significantly with the weakening of winds impinging on the mountain of southern HNI. On the other hand, with the negative perturbation winds

advancing from ICP toward HNI, some compensating downward motion is induced above the boundary layer over southern HNI, causing low-level stabilization. These two processes, both related to the inertial oscillations over ICP, causes the weakening and eventual dissipation of rainfall on southern HNI in the afternoon.

5. Summary and Conclusions

Convective rainfall on HNI off the coast of south China as well as its pronounced diurnal variations have drawn attention of several recent studies. Most such studies have focused on precipitation in northern HNI, which is to the lee of the mountains in the southern part of the Island when it is under prevailing southwesterly EASM flows. In June right after the onset of EASM, precipitation peak typically appears in the afternoon in northern part of the Island, but in the southern part near the coast precipitation exhibits a trimodal pattern with an early-morning peak, a weaker afternoon peak, and an unusual around-noon peak. The prevailing view is that island-scale land and sea breezes dominate the diurnal change of convective rainfall during EASM season on the entire HNI, and are responsible for the early-morning and afternoon rainfall peaks (Liang & Wang, 2017; Zhu et al., 2017). The unusual around-noon peak has not received much attention in comparison and its cause is unclear. Studies on early morning rainfall in southern China have also suggested that boundary layer inertial oscillations are responsible for enhanced onshore flows, and the interactions of such flows with the coastline and coastal mountains can produce enhanced precipitation. It is however unclear how inertial oscillations can form within marine boundary layer where the sea surface temperature does not have much diurnal variations. The expected early morning peak of boundary layer LLJ does not explain the peak rainfall near noon in southern HNI either.

A representative case of 19–20 June 2017 is chosen to investigate the associated mechanisms through a convection-permitting numerical simulation. In the case, rainfall near the southern coast of HNI is initiated in the morning and reaches peak intensity around noon and dissipates in the afternoon. Clockwise rotation in the low-level winds is observed over southern HNI and the upstream ocean. Based on the analysis of modeling results, we summarize the underlying mechanisms in a conceptual model shown in Figure 15.

In the morning (Figure 15a), boundary layer winds form a nocturnal LLJ which reaches peak speed before 06 LST over the plain of ICP, as explained by the Blackadar inertial oscillation theory for boundary layer over land. An orographic gap is located across the coastal Annamite Mountain range right upstream of HNI. The LLJ accelerates as it passes through the gap and the acceleration is further aided by the downslope flow on the leeside with a stable condition near the surface, leading to an especially strong LLJ peaking at 07 LST and 09 LST at and off the coast of ICP. The inertial-oscillation-enhanced boundary layer winds associated with the LLJ core are advected downstream toward HNI by the gap-enhanced flow, at a speed of about 13 m s^{-1} in this case as estimated from a Hovmueller diagram, and reaching offshore of HNI at 11 LST and impinging on the coastal mountains of HNI at around 12 LST. Therefore, in the morning hours, a vertical perturbation circulation (the red vertical circulation in Figure 15a), whose descending and ascending branches are near the ICP and HNI coasts respectively, is established across the strait between ICP and HNI. The lifting of the enhanced low-level southwesterly flows by the coastal mountains initiates convection in southern HNI as early as 10 LST, but the rainfall intensity peaks at 12 LST.

It is the opposite in the afternoon (Figure 15b). During the day, boundary layer winds weaken over the inland plain of ICP due to daytime mixing, and upslope winds also develop on the lee slope of the coastal mountains of ICP. The weakened southwesterly winds are transported downstream toward HNI. By 14 LST, the LLJ over the strait between ICP and HNI has weakened significantly. Such negative low-level perturbation induces a reversed vertical perturbation circulation (the red vertical circulation in Figure 15b) and hence descent near and at the coast of southwesterly HNI. The descent causes low-level stabilization therefore rainfall dissipates quickly afternoon.

Finally, we point out while we believe the mechanisms proposed in this paper are general, more cases should be studied in the future to confirm such a belief.

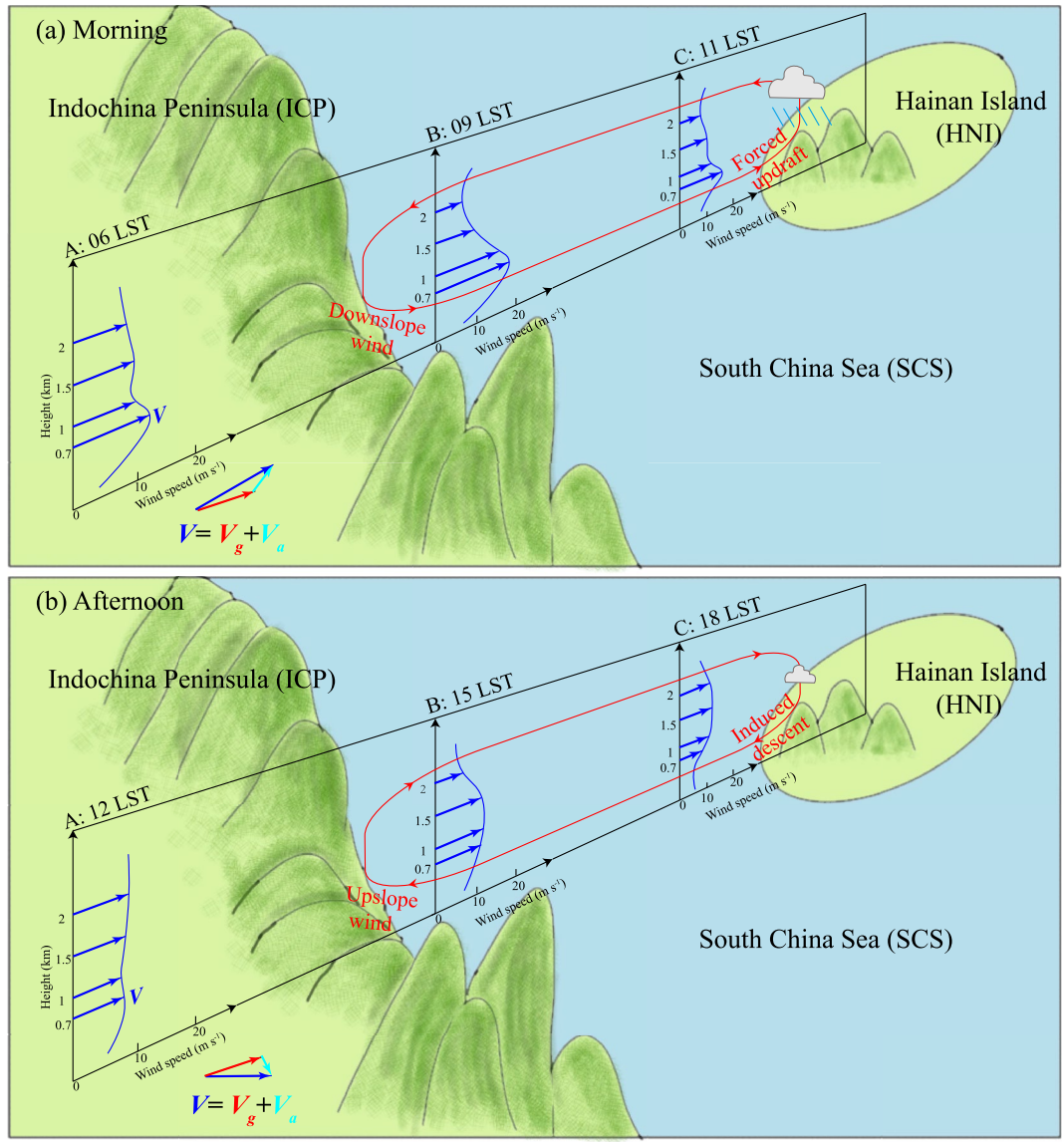

Figure 15. Schematic formation (a) and dissipation (b) mechanisms of convective rainfall on the windward side of Hainan Island (HNI). The low-level wind profiles in specific times and locations show that the layer low-level jet at 700 m MSL intensifies in the morning (a) and weakens in the afternoon (b) due to boundary layer inertial oscillations over Indochina Peninsula (ICP), and transports toward HNI. The red, blue, and cyan vectors at the bottom of each panel represent the geostrophic wind (V_g), actual wind (V), and ageostrophic wind (V_a) on 925 hPa or 700 m MSL at point A, respectively. The red loops in the cross sections represent the secondary vertical circulations across the strait, which are driven by boundary layer inertial oscillations over ICP and have opposite directions in the morning and afternoon. In the morning (a), the nocturnal downslope wind near the coast of ICP and the forced updraft on the windward side of HNI are the descending and ascending branches of the circulation. In the afternoon (b), the daytime upslope wind near the coast of ICP and the induced descent on the windward side of HNI by the approaching negative perturbation winds constitute the ascending and descending branches of the opposite circulation. The locations of A, B, and C correspond to those in Figure 7a.

Data Availability Statement

The WRF-simulated products, the merged CMORPH rainfall and the sounding data of Sanya station are available online (https://doi.org/10.7910/DVN/7ME5QG). The sounding data of Sanya station (WMO identification number: 59948) is retrieved from https://rda.ucar.edu/datasets/ds370.1.

Acknowledgments
This work was supported by the National Key Research and Development Program of China (2018YFC1507303) and the Natural Science Foundation of China (41730965). The first author acknowledges schematic drawing by his daughter Minxian Wang, assistance from fellow student Shiwei Sun, and support from supervisors Minying Gong and Zhunan Cui at work.

References

Bai, L., Chen, G., & Huang, L. (2020). Image processing of radar mosaics for the climatology of convection initiation in South China. *Journal of Applied Meteorology and Climatology*, *59*(1), 65–81. https://doi.org/10.1175/jamc-d-19-0081.1

Blackadar, A. K. (1957). Boundary layer wind maxima and their significance for the growth of nocturnal inversions. *Bulletin of the American Meteorological Society*, *38*(5), 283–290. https://doi.org/10.1175/1520-0477-38.5.283

Chen, G., Lan, R., Zeng, W., Pan, H., & Li, W. (2018). Diurnal variations of rainfall in surface and satellite observations at the monsoon coast (South China). *Journal of Climate*, *31*(5), 1703–1724. https://doi.org/10.1175/jcli-d-17-0373.1

Chen, X., Zhang, F., & Zhao, K. (2016). Diurnal variations of the land–sea breeze and its related precipitation over South China. *Journal of the Atmospheric Sciences*, *73*(12), 4793–4815. https://doi.org/10.1175/jas-d-16-0106.1

Chen, X., Zhao, K., Ming, X., Bowen, Z., Xuanxuan, H., & Weixin, X. (2015). Radar-observed diurnal cycle and propagation of convection over the Pearl River Delta during Mei-Yu season. *Journal of Geophysical Research: Atmospheres*, *120*(24), 12557–12575. https://doi.org/10.1002/2015JD023872

Chen, X., Zhao, K., & Xue, M. (2014). Spatial and temporal characteristics of warm season convection over Pearl River Delta region, China, based on 3 years of operational radar data. *Journal of Geophysical Research: Atmospheres*, *119*(22), 12447–412465. https://doi.org/10.1002/2014JD021965

Crosman, E. T., & Horel, J. D. (2010). Sea and lake breezes: A Review of numerical studies. *Boundary-Layer Meteorology*, *137*(1), 1–29. https://doi.org/10.1007/s10546-010-9517-9

Ding, Y., & Chan, J. C. L. (2005). The East Asian summer monsoon: An overview. *Meteorology and Atmospheric Physics*, *89*(1), 117–142. https://doi.org/10.1007/s00703-005-0125-z

Du, Y., & Chen, G. (2019). Climatology of low-level jets and their impact on rainfall over Southern China during the early-summer rainy season. *Journal of Climate*, *32*(24), 8813–8833. https://doi.org/10.1175/jcli-d-19-0306.1

Du, Y., Chen, G., Han, B., Mai, C., Bai, L., & Li, M. (2020). Convection initiation and growth at the coast of South China. Part I: Effect of the marine boundary layer jet. *Monthly Weather Review*, *148*(9), 3847–3869. https://doi.org/10.1175/mwr-d-20-0089.1

Durran, D. R. (1986). Another look at downslope windstorms. Part I: The development of analogs to supercritical flow in an infinitely deep, continuously stratified fluid. *Journal of the Atmospheric Sciences*, *43*(21), 2527–2543. https://doi.org/10.1175/1520-0469(1986)043<2527:aladwp>2.0.co;2

Fu, P., Zhu, K., Zhao, K., Zhou, B., & Xue, M. (2019). Role of the nocturnal low-level jet in the formation of the morning precipitation peak over the Dabie Mountains. *Advances in Atmospheric Sciences*, *36*(1), 15–28. https://doi.org/10.1007/s00376-018-8095-5

Gaberšek, S., & Durran, D. R. (2004). Gap flows through idealized topography. Part I: Forcing by large-scale winds in the nonrotating limit. *Journal of the Atmospheric Sciences*, *61*(23), 2846–2862. https://doi.org/10.1175/jas-3340.1

Holton, J. R. (1967). The diurnal boundary layer wind oscillation above sloping terrain. *Tellus*, *19*(2), 199–205. https://doi.org/10.1111/j.2153-3490.1967.tb01473.x

Hong, S.-Y., Noh, Y., & Dudhia, J. (2006). A new vertical diffusion package with an explicit treatment of entrainment processes. *Monthly Weather Review*, *134*(9), 2318–2341. https://doi.org/10.1175/mwr3199.1

Iacono, M. J., Delamere, J. S., Mlawer, E. J., Shephard, M. W., Clough, S. A., & Collins, W. D. (2008). Radiative forcing by long-lived greenhouse gases: Calculations with the AER radiative transfer models. *Journal of Geophysical Research*, *113*(D13), D13103. https://doi.org/10.1029/2008jd009944

Jiménez, P. A., Dudhia, J., González-Rouco, J. F., Navarro, J., Montávez, J. P., & García-Bustamante, E. (2012). A revised scheme for the WRF surface layer formulation. *Monthly Weather Review*, *140*(3), 898–918. https://doi.org/10.1175/mwr-d-11-00056.1

Joyce, R. J., Janowiak, J. E., Arkin, P. A., & Xie, P. (2004). CMORPH: A method that produces global precipitation estimates from passive microwave and infrared data at high spatial and temporal resolution. *Journal of Hydrometeorology*, *5*(3), 487–503. https://doi.org/10.1175/1525-7541(2004)005<0487:camtpg>2.0.co;2

Kong, H., Zhang, Q., Du, Y., & Zhang, F. (2020). Characteristics of coastal low-level jets over Beibu Gulf, China, during the early warm season. *Journal of Geophysical Research: Atmospheres*, *125*(14), e2019JD031918. https://doi.org/10.1029/2019jd031918

Li, J., Li, N., & Yu, R. (2019). Regional differences in hourly precipitation characteristics along the western coast of South China. *Journal of Applied Meteorology and Climatology*, *58*(12), 2717–2732. https://doi.org/10.1175/jamc-d-19-0150.1

Liang, Z., & Wang, D. (2017). Sea breeze and precipitation over Hainan Island. *Quarterly Journal of the Royal Meteorological Society*, *143*(702), 137–151. https://doi.org/10.1002/qj.2952

Livneh, B., Restrepo, P. J., & Lettenmaier, D. P. (2011). Development of a unified land model for prediction of surface hydrology and land–atmosphere interactions. *Journal of Hydrometeorology*, *12*(6), 1299–1320. https://doi.org/10.1175/2011jhm1361.1

Shen, Y., Zhao, P., Pan, Y., & Yu, J. (2014). A high spatiotemporal gauge-satellite merged precipitation analysis over China. *Journal of Geophysical Research: Atmospheres*, *119*(6), 3063–3075. https://doi.org/10.1002/2013JD020686

Skamarock, W. C., Klemp, J. B., Dudhia, J., Gill, D. O., Barker, D. M., Wang, W., & Powers, J. G. (2008). A description of the Advanced Research WRF version 3 [Software]. note475+. Retrieved from https://www2.mmm.ucar.edu/wrf/users/download/

Thompson, G., Field, P. R., Rasmussen, R. M., & Hall, W. D. (2008). Explicit forecasts of winter precipitation using an improved bulk microphysics scheme. Part II: Implementation of a new snow parameterization. *Monthly Weather Review*, *136*(12), 5095–5115. https://doi.org/10.1175/2008mwr2387.1

Wang, C., Zhao, K., Huang, A., Chen, X., & Rao, X. (2021). The crucial role of synoptic pattern in determining the spatial distribution and diurnal cycle of heavy rainfall over the South China coast. *Journal of Climate*, *34*(7), 2441–2458. https://doi.org/10.1175/jcli-d-20-0274.1

Xue, M., Luo, X., Zhu, K., Sun, Z., & Fei, J. (2018). The controlling role of boundary layer inertial oscillations in Meiyu frontal precipitation and its diurnal cycles over China. *Journal of Geophysical Research: Atmospheres*, *123*(10), 5090–5115. https://doi.org/10.1029/2018jd028368

Yin, S., Chen, D., & Xie, Y. (2009). Diurnal variations of precipitation during the warm season over China. *International Journal of Climatology*, *29*(8), 1154–1170. https://doi.org/10.1002/joc.1758

Yu, R., Zhou, T., Xiong, A., Zhu, Y., & Li, J. (2007). Diurnal variations of summer precipitation over contiguous China. *Geophysical Research Letters*, *34*(1), L01704. https://doi.org/10.1029/2006GL028129

Zhang, Y., Xue, M., Zhu, K., & Zhou, B. (2019). What is the main cause of diurnal variation and nocturnal peak of summer precipitation in Sichuan Basin, China? The key role of boundary layer low-level jet inertial oscillations. *Journal of Geophysical Research: Atmospheres*, *124*(5), 2643–2664. https://doi.org/10.1029/2018JD029834

Zhang, Z., Cai, X., Song, Y., & Kang, L. (2014). Statistical characteristics and numerical simulation of sea land breezes in Hainan Island (in Chinese). *Journal of Tropical Meteorology*, *30*(02), 270–280. https://doi.org/10.16555/j.1006-8775.2014.03.009

Zhu, L., Chen, X., & Bai, L. (2020). Relative roles of low-level wind speed and moisture in the diurnal cycle of rainfall over a tropical Island under monsoonal flows. *Geophysical Research Letters*, *47*(8), e2020GL087467. https://doi.org/10.1029/2020gl087467

Zhu, L., Meng, Z., Zhang, F., & Markowski, P. M. (2017). The influence of sea- and land-breeze circulations on the diurnal variability in precipitation over a tropical Island. *Atmospheric Chemistry and Physics*, *17*(21), 13213–13232. https://doi.org/10.5194/acp-17-13213-2017